Three-dimensional, distendable bladder phantom for optical coherence tomography and white light cystoscopy

Kristen L. Lurie
Gennifer T. Smith
Saara A. Khan
Joseph C. Liao
Audrey K. Ellerbee

Three-dimensional, distendable bladder phantom for optical coherence tomography and white light cystoscopy

Kristen L. Lurie,[a,†] **Gennifer T. Smith,**[a,†] **Saara A. Khan,**[a] **Joseph C. Liao,**[b,c] **and Audrey K. Ellerbee**[a,*]
[a]Stanford University, Department of Electrical Engineering, Stanford, California 94305
[b]Stanford University School of Medicine, Department of Urology, Stanford, California 94305
[c]Veterans Affairs Palo Alto Health Care System, Palo Alto, California 94304

Abstract. We describe a combination of fabrication techniques and a general process to construct a three-dimensional (3-D) phantom that mimics the size, macroscale structure, microscale surface topology, subsurface microstructure, optical properties, and functional characteristics of a cancerous bladder. The phantom also includes features that are recognizable in white light (i.e., the visual appearance of blood vessels), making it suitable to emulate the bladder for emerging white light + optical coherence tomography (OCT) cystoscopies and other endoscopic procedures of large, irregularly shaped organs. The fabrication process has broad applicability and can be generalized to OCT phantoms for other tissue types or phantoms for other imaging modalities. To this end, we also enumerate the nuances of applying known fabrication techniques (e.g., spin coating) to contexts (e.g., nonplanar, 3-D shapes) that are essential to establish their generalizability and limitations. We anticipate that this phantom will be immediately useful to evaluate innovative OCT systems and software being developed for longitudinal bladder surveillance and early cancer detection. © *The Authors.*

1 Introduction

Optical coherence tomography (OCT) is a high-resolution imaging technique that has shown great promise as a standalone modality for endoscopic applications[1,2] and as an adjunct technology to traditional, white light endoscopy.[3–5] Existing tissue phantoms, however, while useful for many imaging studies, largely fail to mimic key properties of organs that are visible with endoscopic OCT. For example, one phantom designed for acoustic radiation force-optical coherence elastography of the bladder wall[6] mimics bulk optical properties of the bladder but lacks the multilayered structure that is necessary for OCT to distinguish the cancerous tissue; other characteristic features of the bladder, including its rugged surface texture and macroscale structure [i.e., three-dimensional (3-D) shape], are also missing.

Most OCT tissue phantoms model tubular organs or flat areas of organs.[7–10] Thus, to accelerate the development of OCT technology for emerging endoscopic applications, such as for large, irregularly shaped, internal organs, new strategies to fabricate phantoms that can better mimic the macroscale structure, microscale surface topology, subsurface microstructure, optical properties, and compliance of *in vivo* organs are necessary. Additionally, strategies to effectively model the diseased tissue in these organs would enable such phantoms to validate the clinical utility of emerging OCT prototypes.

We are interested in the application of OCT to image the bladder: bladder cancer is the fourth most common cancer in men and is estimated to be responsible for 15,210 deaths in 2013.[11] While OCT has shown significant potential for the early detection of bladder cancer when combined with white light cystoscopy (WLC),[12–15] its development as a tool for comprehensive bladder imaging and automated disease detection is hampered by the lack of suitable large-animal models—or adequate phantoms—to test new hardware and software designs. For example, a phantom that effectively models breathing artifacts or variable distention pressures could facilitate the development of coregistration algorithms to make the use of OCT practical for longitudinal surveillance as a complement to WLC, the current gold standard for bladder cancer diagnosis.[16]

To the best of our knowledge, no phantom exists for OCT imaging of healthy or diseased bladders that simultaneously mimics its multilayered structure, optical properties, macroscale 3-D structure, microscale surface topology, and elastic compliance, although various individual efforts have been described to implement a subset of these features.[8,10,17–25] Moreover, many of the techniques used to generate these phantoms neither scale well nor generalize easily to new contexts.

In this work, we describe a combination of fabrication techniques and a general process to construct a 3-D phantom of the diseased bladder that incorporates all the aforementioned characteristics, thus emulating features visible in endoscopic OCT images. In so doing, we demonstrate the first 3-D OCT phantom

---

*Address all correspondence to: Audrey K. Ellerbee, E-mail: audrey@ee.stanford.edu

†These authors contributed equally to this work.

for bladder tissue that includes features that are recognizable in WLC (i.e., the visual appearance of blood vessels). We also enumerate the nuances of applying certain known fabrication techniques—such as spin coating[18]—to contexts (e.g., nonplanar, 3-D shapes) that are essential to establish their generalizability and limitations. The fabrication process we described has broad applicability and can be generalized to conceive OCT phantoms for other kinds of tissues[26–29] or phantoms for other imaging modalities.[30,31]

2 Relevant Imaging Features of Healthy and Diseased Bladders

In general, the external appearance of the bladder resembles a horizontally elongated ovoid, but its shape may vary depending on its position relative to other organs. During OCT imaging, the surface of the distended bladder wall appears rough due to the texture of the stretched out folds of the bladder wall. The variations in height from a plane within the field of view of our OCT system (2.5 mm^2) are on the order of a few hundred microns. Morphologically, the bladder wall consists of four distinct layers, but only the top three layers—the urothelium, lamina propria, and muscularis propria—are visible in OCT images. The typical thickness and coefficient of attenuation due to scattering (at 1310 nm) of these layers are 50 μm, 400 μm, 1.6 mm (Ref. 32) and 0.49 ± 0.25, 2.0 ± 0.7, and $1.38 \pm 0.7 \text{ mm}^{-1}$ (Ref. 6), respectively, assuming negligible attenuation due to absorption. The actual thicknesses of these layers depend on their location in the bladder and the amount of distention.

When filled with fluid, the distended bladder can enlarge to 15 times its decompressed volume,[33,34] reaching a capacity of approximately 400 cc or more.[35] Visually, distention leads to an apparent thinning of the layers. Additionally, the appearance of the layers is also affected by the disease: the urothelium, lamina propria, and muscularis propria are visually distinct in healthy tissue, but the layered structure of the bladder wall is disrupted in the setting of cancer. Higher stage cancers are associated with fewer distinct layers; thus, visibility of the layers is a key identifying feature for staging and identifying tumors with OCT that may be invisible with WLC (e.g., carcinoma *in situ*).[5,15]

3 Methods and Experimental Design

3.1 General Overview

The complexity of a 3-D, tissue-mimicking phantom with a multilayered structure, varying optical properties, macroscale 3-D shape, microscale surface topology, and elastic compliance necessitated that we should engage and develop a number of different fabrication techniques (Table 1). We chose to construct the phantom from poly(dimethylsiloxane) (PDMS, Sylgard 184, Midland, Michigan) for several reasons: (1) it is easy to form into arbitrary, complex shapes; (2) it possesses tunable, elastic properties; (3) it is amenable to additives that can be used to tune its optical properties; (4) it has a sufficiently low viscosity to enable spinning into thin layers; and (5) it is thermally curable, which provides some control over the curing process. To increase the compliance and distendability of the phantom, we used a 20∶1 ratio of PDMS base to curing agent.

Table 1 Fabrication techniques employed in the construction of a bladder phantom possessing the listed imaging features of interest to optical coherence tomography (OCT) and white light cystoscopy (WLC).

	Technique	Feature
A	Three-dimensional (3-D) printing	3-D shape
B	Particle dispersion	Optical scattering
C	Sandwich molding	Thick layers
D	Spin coating	Thin layers
E	Embossing	Texture
F	Material excision	Diseased states
G	Inking	Vessels
H	Off-ratio bonding	3-D shape

3.2 Fabrication Techniques

3.2.1 3-D printing (A)

The macroscale 3-D shape of the phantom was created by using 3-D-printed molds designed with AutoCAD. Molds were printed using fused deposition modeling with an acrylonitrile butadiene styrene (ABS) plastic (ABS P430, Stratasys, Eden Prairie, Minnesota) that was selected for its low cost and good chemical compatibility with cured PDMS. We discovered that the polylactic acid (PLA) plastic mold alternatives (VisiJet Crystal, 3D systems, Rock Hill, South Carolina), although possible to produce at high resolutions (30 μm versus 250 μm), do not easily allow PDMS to cure on their surfaces unless treated with an acetone adhesive spray (e.g., ModPodge spray adhesive, Plaid Enterprises, Inc., Norcross, Georgia).

To demonstrate the ability to produce phantoms of varying shapes, we produced 3-D-printed molds of a realistic bladder shape (with distinct shapes for the top and bottom halves) and 50- and 100-mm-diameter spheres (with identical top and bottom halves); spheres were used as a rotationally symmetric approximation of a realistic bladder shape. For each mold, we also designed and printed a corresponding "inner mold" to enable sandwich molding and facilitate embossing. The mold pairs were designed such that the inner mold would maintain a fixed gap of controllable size when placed inside the outer mold.

3.2.2 Particle dispersion (B)

To mimic the optical scattering of bladder tissue, titanium dioxide (TiO_2) particles (anatase, Sigma Aldrich, St. Louis, Missouri) were dispersed in PDMS curing agent and mixed with magnetic stir bars for an hour prior to combining with the PDMS base. The required mass ratios of TiO_2:PDMS were calculated based on the protocol of de Bruin et al.[21] and Zha[36] and chosen to match the known coefficients of attenuation due to the scattering of the different layers of the bladder at 1310 nm.[6] The PDMS base and curing agent were mixed by hand and degassed in a vacuum chamber.

3.2.3 Sandwich molding (C)

To create thick layers (>250 μm), 3-D-printed inner molds were first wrapped with aluminum foil (16 μm) to enable the easy removal of the mold from the PDMS layer. Next, the corresponding outer mold was partially filled with degassed PDMS, and the inner mold was carefully inserted (avoiding air bubbles) and secured in place with weights. After curing for 4 h at 60°C, the inner mold and foil were removed. The thickness of the resulting layer depends on the relative sizes of the inner and outer molds. Note that the uniformity of the thickness is limited by the positioning resolution of the molds, which is limited by the resolution of the 3-D printer. Repeated sandwich molding to create multiple layers is possible with the use of successively smaller inner molds.

3.2.4 Spin coating (D)

The 3-D shape attributes of our molds presented unique challenges to achieve the uniform coating for thin layers (30 to 60 μm). That is, the thickness and uniformity of the spun layer depend on the spin speed, spin time, mold size, mold shape, and PDMS viscosity (which is modified by the presence of particle additives). We found that using an unadulterated wafer-spinning protocol[37] on 3-D molds leaves the spun PDMS susceptible to gravity, causing over-accumulation (hypercoating) in topological minima and low coverage (hypocoating) elsewhere.

Therefore, we developed a new spin protocol to mitigate this nonuniformity. First, the base of the outer mold was permanently affixed to a silicon wafer to permit a good contact with the vacuum chuck during spinning. After filling it with PDMS, the mold was spun at the desired speed and time (2 min). We used spin rates from 1000 to 3000 rpm: rates below 1000 rpm do not supply enough centrifugal force to coat the side walls, leading to severe hypocoating in this region; at rates above 3000 rpm, the wafer glued to the mold does not attach well to the vacuum chuck. For the larger molds (bladder, 100-mm sphere), it was necessary to precoat the surface of the mold with PDMS via syringe to prevent the hypocoating. Immediately following the initial spin, the mold was spun at 1000 rpm while irradiated with a temperature-controlled, 250-W heat lamp (BR40, BulbsNLighting, Brooklyn New York, and 11939, Zilla, Franklin, Wisconsin) at 50°C. Spinning at this lower speed prevents drooping after coating and does not significantly affect the resulting layer thickness. Additionally, the heat lamp causes partial curing (i.e., semi-curing); Bisaillon et al. also demonstrates a method using heat curing to achieve uniformly thick layers, though their process is not amenable to fabricate nonluminal organs.[38]

The entire process can be repeated to build additional layers with the same or different optical properties after curing in an oven for 10 min at 60°C. We successfully spin coated up to 15 layers with differing thicknesses and optical properties in a single mold (data not shown). Compared with sandwich molding, using repeated spin coating to build thick layers having the same optical properties is less time efficient and permits only shallow texturing of the surface; however, for thinner layers (at least up to 200 μm), especially those embossed with foil, repeated spin coating creates more uniform layers and leads to a more reliable thickness overall.

Experimental characterization of the spin parameters needed to achieve target layer thicknesses proceeded as follows. For a given outer mold, we spin coated alternating layers of clear PDMS and a TiO_2: PDMS dispersion using spin speeds ranging from 1000 to 3000 rpm. The resulting layered structures were imaged with a commercial spectral-domain-OCT system (TELESTO, ThorLabs, Newton, New Jersey) at various distances from the center of the mold. A custom MATLAB® script was written to extract and measure the physical thicknesses of the layers. When computing the physical thickness from the optical thicknesses obtained with OCT, we used a refractive index of 1.4 for all scattering layers in the phantom, which reflects the assumption that the concentration of TiO_2 is too small to significantly affect the refractive index of the PDMS, as suggested by the Lorentz-Lorenz mixing rule.

3.2.5 Embossing (E)

To mimic the rugged surface texture of bladder tissue, we embossed the surface of semi-cured PDMS through direct contact with arbitrarily crumpled foil. The inner mold was wrapped with the crumpled foil prior to inserting it into the outer mold when sandwich molding. For embossing layers created by spin coating, it was most effective to first press the crumpled foil into semi-cured PDMS and then insert the inner mold with added pressure.

The optimal semi-cure time—that which hardens the PDMS enough to prevent drooping but provides sufficient tackiness to enable the transfer of the surface contour of the foil—was experimentally determined to depend on spin speed, spin time, and mold size. Thin layers of varying thicknesses and coefficients of attenuation due to scattering were generated by spin coating different molds, as previously described. Each layer was irradiated with a heat lamp at 50°C for 30 s, after which its tackiness was qualitatively assessed by gently touching it with a gloved finger or small piece of foil. The PDMS was visually assessed for signs of drooping and subjected to additional semi-curing in increments of 30 s until the appropriate amount of tackiness was achieved. Drooping refers to the tendency for the spun PDMS to succumb to gravity, causing over-accumulation in topological minima and low coverage elsewhere, leading to nonuniformity in layer thickness. Drooping manifests visually as the newly applied PDMS layer sliding down the mold toward the topological minima.

It is also possible to apply well-defined patterns to thin and thick layers of the phantom by embossing the surface with a mold. Others have demonstrated this step for OCT phantoms, though their texturing was embossed on a planar or near-planar surface.[8,20,21,39] For thick layers, an inner mold bearing the desired pattern was wrapped with smoothed aluminum foil to facilitate the removal after curing. The inner mold was then inserted into the outer mold containing PDMS and cured. Thin layers were semi-cured during the spin coating prior to embossing, similar to the foil embossing procedure. The lower adhesion between the PDMS and mold when patterning thin layers obviated the need for foil.

3.2.6 Material excision (F)

To simulate the appearance of tumors that manifest as disruption of the layered structure, we selectively excised portions of cured layers with a scalpel prior to fabricating new layers on top of them. Excised regions were partially filled by a hand-held syringe with material possessing the same scattering characteristics as that intended for the subsequent layer. The regions were

then cured for 10 min via heat lamp, while the mold was angled to prevent drooping.

3.2.7 Inking (G)

The addition of TiO_2 to naturally transparent PDMS gives it a white, featureless appearance. To create arbitrary colored regions consistent with features that are compatible with white light imaging (e.g., vessels), we inked the PDMS using a water-based paint pen (Sharpie, Oak Brook, Illinois). To prevent the smearing or removal during subsequent use of the phantom, inking was always followed by spin coating PDMS either with or without dispersed particles. The spin-coating step we introduced is essential to overcome the well-known problem of permanently marking the surface of hydrophobic PDMS.[40]

3.2.8 Off-ratio bonding (H)

Complex, irregularly shaped pieces of PDMS can be bonded together effectively using uncured PDMS as an adhesive in an off-ratio bonding technique.[41,42] In brief, two cured components of PDMS are aligned edge-to-edge, creating a seam. Uncured PDMS comprising a base to curing agent ratio that differs from that used to fabricate the individual components is applied to the seam and then cured at 60°C.

3.3 Construction of the Bladder Phantom

We applied the techniques described above to fabricate a multi-layered PDMS phantom resembling a human bladder in shape and size (Fig. 1). The phantom consisted of three components: two halves of differing shapes and a piece of silicone tubing.

A 3-D model of the bladder was created from a point cloud derived from a human CT scan collected previously by the Human Photonics Laboratory at the University of Washington.[25] The point cloud was transformed into a 3-D model using MeshLab (3D-CoForm, Brighton, England) and Mesh Enabler (Inventor, AutoDesk, San Rafael, California) to create a 3-D mesh and matching solid, respectively. The solid was then transformed into designs for inner and outer 3-D-printed molds for the two distinct halves with CAD. Steps to fabricate multiple layers, diseased states, and vasculature were performed concurrently for both halves.

All layers were made from PDMS containing an appropriate dispersion of TiO_2 particles. The percentages by mass of TiO_2 used for the muscularis propria, lamina propria, and urothelium were 0.1486%, 0.2131%, and 0.0561%, respectively. The muscularis propria layer was fabricated by sandwich molding with a designed gap thickness of 1.5 mm between the inner and outer molds for both halves. Foil embossing was used to add arbitrary texture to the surface of the layer. The lamina propria layer was then fabricated through repeated spin coating of a TiO_2 + PDMS dispersion (eight total layers) and foil embossing to add arbitrary texture. We chose to use the spin coating, rather than sandwich molding, to fabricate the lamina propria, because the combined sandwich molding and foil embossing techniques did not permit fabrication of such thin layers with well-defined thicknesses. Next, diseased states at random locations were created by material excision in both halves; this process mimics flat tumors with a stage T2 or greater. Free-hand drawing was performed to ink the layer to mimic the appearance of vasculature. A thin urothelium layer was added last by spin coating a TiO_2 + PDMS dispersion on top of the inked layer. Foil embossing was again used to add arbitrary texture to the surface of the layer.

The two multilayered halves were combined using off-ratio bonding. Prior to application of the PDMS adhesive, the edges of the two halves were aligned by placing them around a sand-filled balloon that remained in place during bonding. A small hole was cut in the bottom of the phantom to assist with removing the balloon after curing; this hole was later used to insert and bond a silicone tube with an inner diameter of 7 mm and length of 80 mm to form the urethral opening. The tube was affixed by off-ratio bonding.

3.4 Visual Comparison with Bladder Tissue

3.4.1 Preparation of samples

Healthy bladder tissue was harvested from a female pig euthanized as part of an unrelated study; pig bladder tissue is known to closely mimic the properties of human bladder in terms of composition and biomechanical properties.[43] Human bladder tissues were obtained as part of a research protocol approved by the Stanford University Institutional Review Board. After informed consent, both normal-appearing and tumor tissues were obtained from a human subject during a standard transurethral resection of bladder tumor procedure. The tumor tissue was
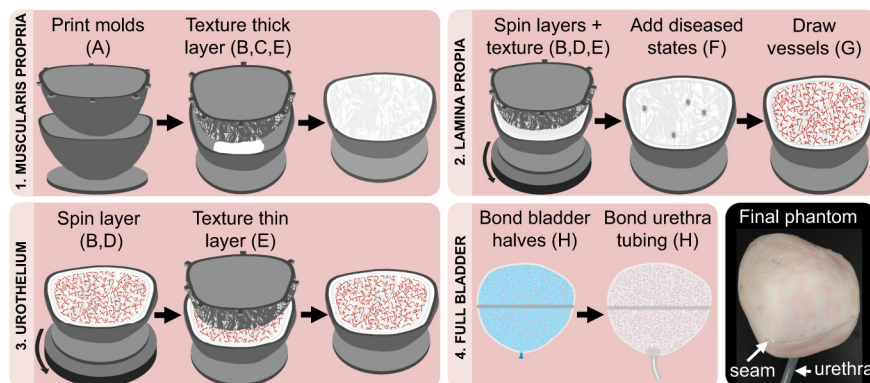

Fig. 1 Representative steps to fabricate a full-bladder phantom. The sequence of steps 1 to 3 is performed twice—once for each half of the bladder—before step 4. Letters refer to techniques listed in Table 1.

pathologically confirmed to be a high-grade, stage T1 urothelial carcinoma of the bladder. During imaging, tissue samples were immersed in a 0.9% w/v solution of sodium chloride during imaging to maintain the osmotic pressure in the blood vessels and to reduce the refractive index mismatch between the tissue surface and surrounding medium.

3.4.2 *OCT and white light imaging*

Healthy and diseased bladder tissues were imaged to compare the thicknesses, surface topology, and relative contrast between each layer with our bladder phantom. Cystoscopic images were collected from a clinical fluorescence cystoscopy system (Photodynamic Diagnostic D-Light C System, Karl Storz Endoscopy, El Segundo, California). The OCT images were collected with a commercial SD-OCT system (center wavelength 1325 nm, TELESTO, ThorLabs) at various distances from the edge of the bladder to measure the uniformity of the layer thickness. The bladder phantom was immersed in water for OCT imaging and saline for cystoscopic imaging.

3.4.3 *Distention of the bladder phantom*

To demonstrate the ability of our bladder phantom to distend, we subjected the phantom to varying air pressures. The imaging end of the cystoscope was first inserted through the urethra and sealed by tightening a hose clamp around the urethra. The cystoscope was connected to a transurethral resection of bladder tumor (TURBT) y-tubing connector via latex tubing. The two y-tubing input tubes were then connected to controllable air and vacuum valves for distention or deflation. We chose to distend the bladder with air rather than the typical liquids used in clinical settings to better show the range of distendability of the phantom. Note that the distention with liquid is possible using a clinical irrigation pump.
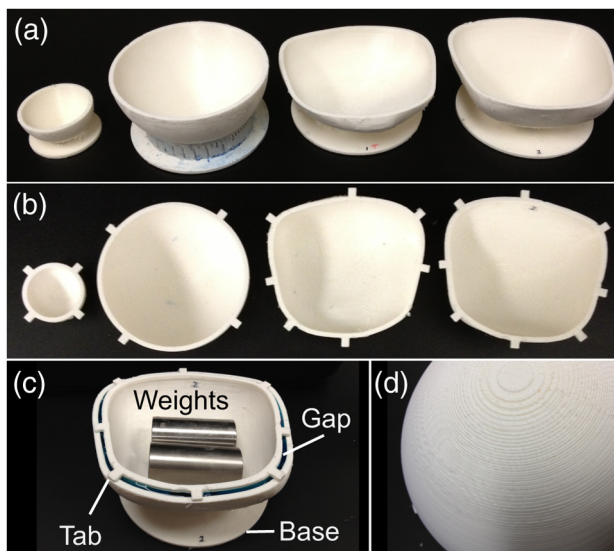

Fig. 2 Collection of molds we tested: (a) Outer molds and (b) corresponding inner molds for the 50-mm sphere, 100-mm sphere, top half of bladder, and bottom half of bladder. (c) Visualization of the gap for sandwich molding (shows the flat base, alignment tabs, and positioning of weights used during molding). (d) Closeup of the textured surface of the molds caused by the finite resolution of the three-dimensional (3-D) printer.

4 Results and Discussion

The 3-D printed molds we created varied in size and shape according to the specified mesh designs. Figure 2 shows an image of the collection of molds we tested. All molds exhibited a patterned texture due to the limited resolution of the 3-D printer and ABS-like plastic [Fig. 2(d)]; however, this texture was not transferred to the layers when covered in foil for embossing and can be smoothed using acetone. Two purposeful design features are worth noticing: (1) a flat base added to the outer mold, facilitated gluing it to a wafer for spin coating; and (2) alignment tabs on the inner and outer molds enabled repeatable and controlled placement of the inner mold within the outer mold at a fixed gap distance.

4.1 *Effect of 3-D Mold Shape on Achievable Layer Thicknesses*

The thickness of layers created by sandwich molding was controlled by the CAD design of the gap distance. For thin layers formed by spin coating, however, the achievable thickness varied as a function of mold shape, spin speed, and PDMS viscosity. The inset of Fig. 3(a) shows a representative, segmented OCT-B-scan image of nine alternating layers of clear PDMS and $TiO_2 + PDMS$ (0.1486% mass ratio) spun inside the outer mold of the bottom half of the bladder. The clear layers function solely to facilitate the segmentation and measurement of the thicknesses of the scattering layers. Each pair of clear and scattering layers was fabricated by applying a unique spin speed for 2 min followed by semi-curing at 1000 rpm according to the values described in Sec. 4.2.

Figure 3(a) plots the median physical thicknesses of the scattering layers as a function of spin speed assuming a refractive index of 1.4 for each layer. As expected, the layer thickness decreased with increasing spin speed for all mold shapes. (One exception is the top half of the bladder at 2500 rpm; this discrepancy may be due its irregular shape.) When measuring the thicknesses from mold shapes, a strip was cut along the full circumference of the mold (or the diameter in the case of the wafer) and flattened for imaging. Images were then taken at regular intervals along the length of the strip: every 2.5 mm for the small sphere and every 5 mm for all other shapes. Notably, the range of achievable thicknesses on the 3-D shapes is narrower than that of the wafer for the same range of spin speeds.

Figure 3(b) shows the variation in layer thickness as a function of distance from the center of the base of the mold for the lowest and the highest spin speeds tested (1000 and 3000 rpm). Reported positions (x-axis) are normalized to the length of the cut strip. While the wafers exhibited near-uniform thickness at all locations, the layers formed in 3-D shapes are significantly thicker at the edges—in some cases, the achieved thicknesses are nearly 60 μm larger than the median. For a given spin speed, the thickness increases with distance from the center of the mold. One potential explanation for this is that the steep sidewalls make it difficult for the PDMS to eject from the sidewalls during spinning. Thus, spinning in 3-D shapes posesess two challenges: (1) for highly curved shapes, it is difficult to achieve truly uniform layer thicknesses across the entire shape with a single-spin protocol; and (2) for a given range of spin speeds, the range of achievable thicknesses is compressed compared with wafers (medians of approximately 25 to 45 μm on 3-D molds versus 25 to 60 μm on flat wafers). Future work
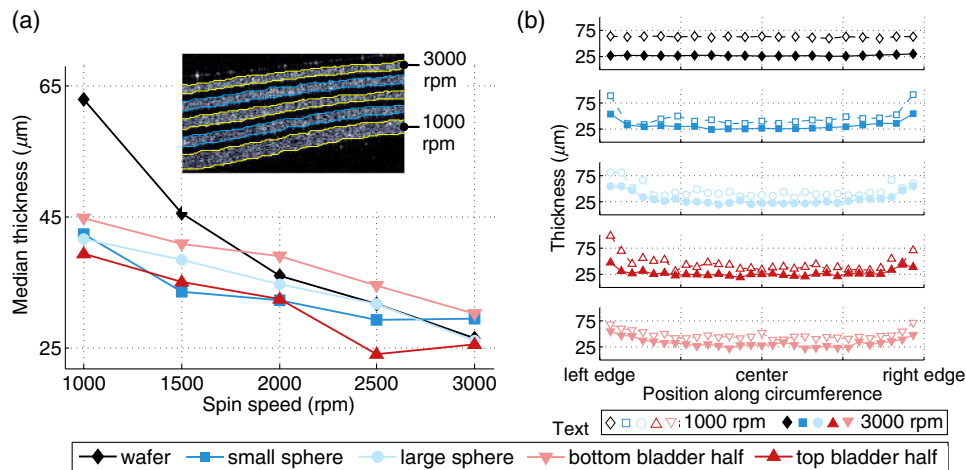
Fig. 3 Physical thickness of spin-coated layers. (a) Median layer thickness versus spin speed for five 3-D shapes. The inset shows a representative OCT-B-scan of multiple layers fabricated on the bottom half of the bladder at different spin speeds. (b) Layer thickness versus spin speed and normalized distance along shape diameter (wafer) or circumference (molds).

could seek to develop new methodologies or spin protocols to address these complex effects.

A minimum thickness of 25 μm, which is attainable with the spin-coating method we described, is more than sufficient to fabricate a layer that mimics the thinnest layer of the bladder; however, thinner layers, as may be desirable for phantoms of other organs, could likely be achieved either by spinning at a faster speed (when smaller molds are used) or by using *tert*-butyl alcohol as a solvent to reduce the viscosity of the PDMS during spin coating.[44] For thick layers, a back-to-back, repeated spin-coating protocol may be necessary. Alternatively, one can consider sandwich molding.

The reported thicknesses correspond to a TiO_2 ratio of 0.1486% by mass (i.e., the ratio used for the muscularis propria layer). Independent of prespin speed, the variation in the obtained thicknesses as a function of TiO_2 ratio was insignificant (data not shown) for the range of TiO_2 mass ratios we used. Table 2 shows the final spin speeds used to achieve bladder wall-mimicking layers in the large bladder mold and compares the desired thickness of each layer with the measured median thickness of the layers in our phantom.

4.2 Effect of 3-D Mold Shape on Layer Texturing

Texturing of layers was accomplished by embossing uncured PDMS following sandwich molding or spin coating. In the case of the latter, an additional semi-curing step was necessary

to prevent drooping of the PDMS during the embossing process. Table 3 lists the experimentally determined times required to achieve the sufficient semi-curing to emboss layers of varying thicknesses in molds of different 3-D shapes. Different layer thicknesses were achieved by varying the spin speeds.

As can be seen, the semi-cure times are a function of both layer thickness (i.e., spin speed) and mold size, but not strictly of mold shape. In general, the semi-cure time decreased with decreasing layer thickness (i.e., increasing spin speeds). For a given thickness, semi-curing generally took longer in large molds than in small molds because the available heat energy was constant while the surface area increased, reducing the irradiance. A decrease in semi-cure time for larger molds may be possible by increasing the heating temperature to increase the irradiance.

Although our methodology to determine the semi-cure time was only semi-quantitative, it is not necessary to determine the exact semi-cure time to fabricate a working phantom. In fact, a range of suitable semi-cure times exists for which the PDMS is solid enough to avoid the hypo- or hypercoating but tacky enough for embossing. Our choice of a 30-s interval for testing semi-cure times was largely one of convenience to ensure that we were able to find a time point within the range of possible cure times.

Figure 4 shows the examples of thick and thin layers textured by foil and mold embossings. In the latter case, our research logo is clearly visible, whereas the surface texture appears

Table 2 Comparison of desired and measured median physical thicknesses in the bladder phantom. The lamina propria is built up with eight spin-coat layers.

	Target thickness (μm)	Median thickness (μm)		Spin speed (rpm)	
		Top half	Bottom half	Top half	Bottom half
Urothelium	50	45.5	47.4	1000	1000
Lamina propria	300 to 400	369.3	382.0	1000 (8×)	1000 (8×)
Muscularis propria	1600	1500	1490	N/A	N/A

Table 3 Semi-cure times in minutes for a poly(dimethylsiloxane) (PDMS) layer as a function of 3-D shape and spin speed.

	Spin speed (rpm)				
	1000	1500	2000	2500	3000
Small sphere	3.5	3	2.5	1.5	1
Large sphere	5.5	5	4.5	4	3.5
Bladder—top half	5.5	5	4.5	4	3.5
Bladder—bottom half	5.5	5	4.5	4	3.5
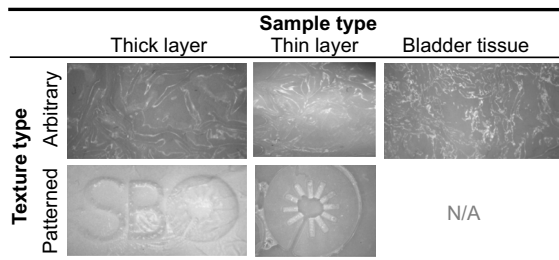
Fig. 4 Examples of thick and thin layers (left and middle columns, respectively) textured by embossing with crumpled foil (top row) or a mold patterned with our laboratory logo "SBO" (bottom row). An image of bladder tissue is presented for comparison with foil embossing (right column). All images are presented in grayscale.

arbitrary in the former. The arbitrary pattern of the crumpled foil closely resembles the texture of bladder tissue (Fig. 4).

4.3 Appearance of the Phantom During Imaging

Figure 5 highlights various visual similarities between our phantom and patient-derived bladder biopsies (normal and cancerous) when viewed by WLC and OCT: (1) The OCT-B-scans show that the layers of our phantom are similar in thicknesses to those found in bladder tissue; however, the current phantom design does not adequately mimic the fibrous appearance of the muscularis propria layer that is evident in real tissue. (2) Muscle-invasive cancer, which is marked by complete disruption of
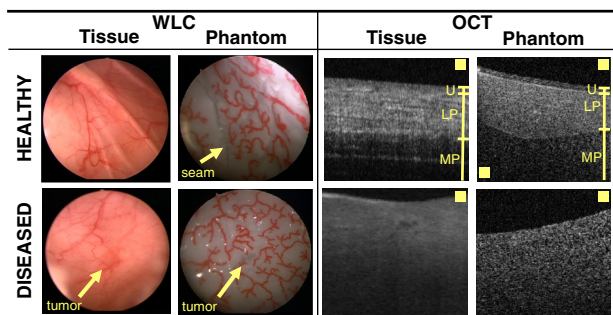
Fig. 5 White light cystoscopy (WLC) (Video 1) and optical coherence tomography (OCT) comparisons of bladder tissue and the bladder phantom. The boxes in OCT-B-scans are 100 μm^2. Individual layers in healthy B-scans are labeled: urothelium (U), lamina propria (LP), and muscularis propria (MP). Note that the WLC and OCT images are not collected from the same locations (MOV, 8.3 MB) [URL: http://dx.doi.org/10.1117/1.JBO.19.3.036009.1]..
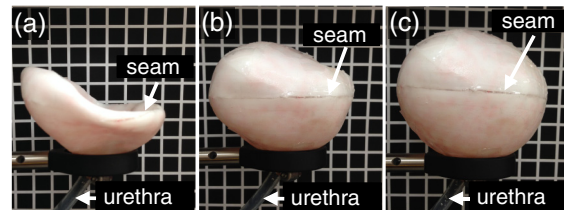
Fig. 6 Exterior of bladder phantom undergoing distention with various air pressures (Video 2): (a) hypodistention, (b) normal distention, and (c) hyperdistention. Grid boxes are approximately 20 × 20 mm² (MOV, 4.1 MB) [URL: http://dx.doi.org/10.1117/1.JBO.19.3.036009.2].

the layered structure in OCT, is possible with the proposed fabrication procedure: both diseased bladder tissue and diseased areas of the phantom have a single-scattering layer without much evidence of subsurface structure. However, modification of our fabrication technique is necessary to model other stages of precancerous and cancerous pathologies. (3) The WLC images reveal the appearance of vessels in both tissue and the phantom, and the appearance of tumors is subtle in both tissue and the phantom under WLC illumination. Note that we do not attempt to mimic a reddish color contrast between the tumor and surrounding tissues (nor do we attempt to mimic the pink color of the bladder tissue), as our goal here was merely to mimic a class of tumors that are nearly invisible to WLC but identifiable by OCT. Our current phantom is capable of doing this. In the future, however, it may be possible to mimic the coloration of tissue by dying the PDMS prior to curing.[45] Additionally, the phantom we created does not contain any tissue-like structures in the urethral tube. However, other works that describe methods to create multilayered phantoms of luminal organs could be adopted to create realistic tissue structures in the tubular regions.[10]

Unlike some phantoms that mimic only the sections of organs, our bladder phantom is fully enclosed except for a urethral opening and is sufficiently large to enable the passage of standard clinical cystoscopes. Thus, our phantom is capable of undergoing both distention and surveillance via WLC. The WLC was performed on a saline-filled bladder phantom (Video 1) by a urology fellow at the VA Palo Alto Health Care System. During the cystoscopy, areas of the bladder wall were examined head-on and along the surface to search for tumors, as is done in clinical cystoscopy. The seam of the phantom is noticeable but occupies only a small portion of the total surface area. The index of refraction mismatch between the phantom (1.4) and the saline (1.33) causes the appearance of specular reflections when the phantom is not viewed obliquely; specular reflections could be minimized by replacing saline with a fluid that has a more similar index of refraction to the phantom. Alternatively, one could try to identify more biologically index-matched materials to build the phantom. In general, the phantom was easy to manipulate and adequately mimicked the appearance and functionality of real bladder tissue. Finally, Fig. 6 shows the still frames from a movie (Video 2) taken of the pressurized bladder phantom. Due to the elasticity of the PDMS, the bladder could be made to contract or stretch when subjected to different air pressures. The apparent 3-D shape of the bladder was a function of the applied pressure.

5 Conclusions

In conclusion, we described a novel combination of techniques to produce the first 3-D bladder phantom for combined OCT

and WLC that presents with multiple layers, is elastically distendable, and incorporates diseased states. The ability to mimic multiple features in a single phantom speaks to the versatility of our fabrication process, which is well suited to fabricate phantoms of other large organs of arbitrary shape. Images of the phantom acquired under realistic conditions validate its potential use for testing new equipment and its ability to incorporate diseased states that may serve as gold standard imaging targets.

Note that we did not attempt to mimic every property of bladder tissue. For example, PDMS has a much higher elastic modulus than normal tissue [1483 kPa (Ref. 7) versus 4.7 kPa (Ref. 46)]. In the future, it may be possible to improve the elastic modulus through the addition of pure PDMS to the curing agent[38,47] when fabricating one or more layers. Additionally, our phantom could be expanded to mimic absorption properties of tissue through the use of molecular absorbers[48] or dyes. Regarding the protocol, while spin coating is most appropriate to mimic organs with a high degree of rotational symmetry, we demonstrated that the process may be adapted for nonrotationally symmetric organs. However, future work should investigate other methods and protocols to further increase the uniformity of thin layers created in 3-D molds.

Overall, the proposed process is capable of creating a 3-D bladder phantom that can be used to simulate realistic imaging conditions. We anticipate that this phantom will be immediately useful to evaluate novel OCT systems and software being developed for longitudinal bladder surveillance and early cancer detection.

References

1. X. D. Li et al., "Optical coherence tomography: advanced technology for the endoscopic imaging of Barrett's esophagus," *Endoscopy* **32**(12), 921–930 (2000).
2. D. C. Adler et al., "Three-dimensional endomicroscopy using optical coherence tomography," *Nat. Photonics* **1**(12), 709–716 (2007).
3. S. Brand et al., "Optical coherence tomography in the gastrointestinal tract," *Endoscopy* **32**(10), 796–803 (2000).
4. B. Shen and G. Zuccaro, "Optical coherence tomography in the gastrointestinal tract," *Gastrointest. Endosc.* **14**(3), 555–571 (2004).
5. S. P. Lerner et al., "Optical coherence tomography as an adjunct to white light cystoscopy for intravesical real-time imaging and staging of bladder cancer," *Urology* **72**(1), 133–137 (2008).
6. O. A. Ejofodomi, V. Zderic, and J. M. Zara, "Tissue-mimicking bladder wall phantoms for evaluating acoustic radiation force-optical coherence elastography systems," *Med. Phys.* **37**(4), 1440–1448 (2010).
7. G. Lamouche et al., "Review of tissue simulating phantoms with controllable optical, mechanical and structural properties for use in optical coherence tomography," *Biomed. Opt. Express* **3**(6), 1381–1398 (2012).
8. Y. M. Liew et al., "Reduction of image artifacts in three-dimensional optical coherence tomography of skin in vivo," *J. Biomed. Opt.* **16**(11), 116018 (2011).
9. G. van Soest, F. Mastik, and A. F. van der Steen, "Polyvinyl alcohol cryogel—tissue mimicking material for vascular optical elastography," in *Biomedical Optics, Technical Digest, TuI33, Optical Society of America*, Washington, DC (2006).
10. C.-E. Bisaillon and G. Lamouche, "Artery phantoms for intravascular optical coherence tomography: diseased arteries," *J. Biomed. Opt.* **18**(9), 96010 (2013).
11. R. Siegel, D. Naishadham, and A. Jemal, "Cancer statistics, 2013," *CA-Cancer J. Clin.* **63**(1), 11–30 (2013).
12. H. Ren et al., "Diagnosis of bladder cancer with microelectromechanical systems-based cystoscopic optical coherence tomography," *Urology* **74**(6), 1351–1357 (2009).
13. Y. T. Pan et al., "Diagnosis of biological tissue morphology and function with endoscopic optical coherence tomography," in *Engineering in Medicine and Biology Conf.*, pp. 7217–7220, IEEE, Shanghai, China (2005).
14. M. J. Manyak et al., "Evaluation of superficial bladder transitional-cell carcinoma by optical coherence tomography," *J. Endourol.* **19**(5), 570–574 (2005).
15. C. A. Lingley-Papadopoulos et al., "Computer recognition of cancer in the urinary bladder using optical coherence tomography and texture analysis," *J. Biomed. Opt.* **13**(2), 024003 (2008).
16. M. N. M. van der Aa et al., "Cystoscopy revisited as the gold standard for detecting bladder cancer recurrence: diagnostic review bias in the randomized, prospective CEFUB trial," *J. Urol.* **183**(1), 76–80 (2010).
17. Y. Bae et al., "Fabrication of a thin-layer solid optical tissue phantom by a spin-coating method: pilot study," *J. Biomed. Opt.* **18**(2), 025006 (2013).
18. J. Baxi et al., "Retina-simulating phantom for optical coherence tomography," *J. Biomed. Opt.* **19**(2), 021106 (2014).
19. C.-E. Bisaillon et al., "Poly(vinyl alcohol) cryogel, multi-layer artery phantoms for optical coherence tomography," *Proc. SPIE* **7906**, 79060J (2011).
20. A. Curatolo, B. F. Kennedy, and D. D. Sampson, "Structured three-dimensional optical phantom for optical coherence tomography," *Opt. Express* **19**(20), 19480–19485 (2011).
21. D. M. de Bruin et al., "Optical phantoms of varying geometry based on thin building blocks with controlled optical properties," *J. Biomed. Opt.* **15**(2), 025001 (2010).
22. T. S. Rowe and R. J. Zawadzki, "New developments in eye models with retina tissue phantoms for ophthalmic optical coherence tomography," *Proc. SPIE* **8229**, 822913 (2012).
23. R. B. Saager et al., "Multi-layer silicone phantoms for the evaluation of quantitative optical techniques in skin imaging," *Proc. SPIE* **7567**, 756706 (2010).
24. P. H. Tomlins et al., "Femtosecond laser micro-inscription of optical coherence tomography resolution test artifacts," *Biomed. Opt. Express* **2**(5), 1319–1327 (2011).
25. W. J. Yoon et al., "Development of an automated steering mechanism for bladder urothelium surveillance," *J. Med. Devices* **3**(1), 011004 (2009).
26. J. Baeten et al., "Development of fluorescent materials for diffuse fluorescence tomography standards and phantoms," *Opt. Express* **15**(14), 8681–8694 (2007).
27. T. Wang et al., "Comparison of pulsed photothermal radiometry, optical coherence tomography and ultrasound for melanoma thickness measurement in PDMS tissue phantoms," *J. Biophotonics* **4**(5), 335–344 (2011).
28. B. Ebrahimi et al., "A perfusion phantom for quantitative medical imaging," *Proc. SPIE* **6913**, 69130W (2008).
29. B. F. Kennedy et al., "Fibrin phantom for use in optical coherence tomography," *J. Biomed. Opt.* **15**(3), 030507 (2010).
30. B. W. Pogue and M. S. Patterson, "Review of tissue simulating phantoms for optical spectroscopy, imaging and dosimetry," *J. Biomed. Opt.* **11**(4), 041102 (2006).
31. C. U. Devi, R. M. Vasu, and A. K. Sood, "Design, fabrication, and characterization of a tissue-equivalent phantom for optical elastography," *J. Biomed. Opt.* **10**(4), 044020 (2005).
32. M. G. Wientjes et al., "Bladder wall penetration of intravesical mitomycin C in dogs," *Cancer Res.* **51**(16), 4347–4354 (1991).
33. R. T. Kershen, K. M. Azadzoi, and M. B. Siroky, "Blood flow, pressure and compliance in the male human bladder," *J. Urol.* **168**(1), 121–125 (2002).
34. B. T. Haylen, "The empty bladder," *Int. Urogynecol. J.* **18**(3), 237–239 (2007).
35. N. Yoshimura and M. B. Chancellor, "Physiology and pharmacology of the bladder and urethra," Chapter 60 in *Campbell-Walsh Urology*, 10th ed., W. McDougal et al., Eds., pp. 1786–1833, Elsevier Inc., Philadelphia (2011).

36. X. Zha, "Image processing of optical coherence tomography for image guided dental drilling," Master's Thesis, Delft University of Technology, Biomechanical Engineering (2011).
37. W. Y. Zhang, G. S. Ferguson, and S. Tatic-Lucic, "Elastomer-supported cold welding for room temperature wafer-level bonding," in *Int. Conf. MEMS*, Vol. 2(c), pp. 741–744, IEEE (2004).
38. C.-E. Bisaillon, M. L. Dufour, and G. Lamouche, "Artery phantoms for intravascular optical coherence tomography: healthy arteries," *Biomed. Opt. Express* **2**(9), 2599–2613 (2011).
39. R. Y. Gu et al., "Variable-sized bar targets for characterizing three-dimensional resolution in OCT," *Biomed. Opt. Express* **3**(9), 2317–2325 (2012).
40. D. C. Trimbach et al., "Hydrophilic elastomers for microcontact printing of polar inks," *Langmuir* **20**(11), 4738–4742 (2004).
41. R. Long et al., "Optofluidic phantom mimicking optical properties of porcine livers," *Biomed. Opt. Express* **2**(7), 1877–1892 (2011).
42. M. A. Eddings, M. A. Johnson, and B. K. Gale, "Determining the optimal PDMS-PDMS bonding technique for microfluidic devices," *J. Micromech. Microeng.* **18**(6), 067001 (2008).
43. S. E. Dahms et al., "Composition and biomechanical properties of the bladder acellular matrix graft: comparative analysis in rat, pig and human," *Br. J. Urol.* **82**(3), 411–419 (1998).
44. J. H. Koschwanez, R. H. Carlson, and D. R. Meldrum, "Thin PDMS films using long spin times or tert-butyl alcohol as a solvent," *PloS One* **4**(2), e4572 (2009).
45. A. Llobera et al., "Monolithic PDMS passband filters for fluorescence detection," *Lab Chip* **10**(15), 1987–1992 (2010).
46. J. W. Lee et al., "Palpation device for the identification of kidney and bladder cancer: a pilot study," *Yonsei Med. J.* **52**(5), 768–772 (2011).
47. A. L. Oldenburg et al., "Magnetomotive contrast for in vivo optical coherence tomography," *Opt. Express* **13**(17), 6597–6614 (2005).
48. T. Moffitt, Y.-C. Chen, and S. A. Prahl, "Preparation and characterization of polyurethane optical phantoms," *J. Biomed. Opt.* **11**(4), 041103 (2006).

Kristen L. Lurie received her AB and BE degrees from Dartmouth College and her MS degree from Stanford University. She is currently a PhD student at Stanford University in the Department of Electrical Engineering.

Gennifer T. Smith received her dual-major BS degree in 2012 from the University of New Mexico in electrical engineering and biology. She is currently a PhD student in electrical engineering at Stanford University.

Saara A. Khan is a PhD electrical engineering student at Stanford University. Her research accomplishments have resulted in several awards, most notably the National Science Foundation Graduate Fellowship and the Stanford Graduate Student Fellowship. She received her BS in 2012 from the University of Maryland in electrical engineering with a focus in electrophysics.

Joseph C. Liao is currently an associate professor of urology at Stanford University and chief of urology at Veterans Affairs Palo Alto Health Care System. He received his MD from Stanford University and completed his postgraduate training in urology at UCLA. He is a board-certified urologist who maintains an active clinical practice focusing on urologic oncology and a research focus on cancer imaging and image-guided surgery.

Audrey K. Ellerbee is an assistant professor of electrical engineering at Stanford University. She received her BSE degree from Princeton University, PhD degree in biomedical engineering from Duke University, and completed her postdoctoral training in chemistry and chemical biology at Harvard University. Her research interests include applications of optics to medicine and biology. In particular, her research focuses on development of translational imaging technologies, such as optical coherence tomography, for use in the clinic or point-of-care settings.